RSC Advances

PAPER

View Article Online
View Journal | View Issue

Cite this: *RSC Adv.*, 2026, **16**, 14083

Research on terahertz multitunable multifunctional absorbers based on graphene and indium antimonide

Baojing Hu, *[a] Changjin Cai,[a] Ke Li[b] and Weifeng Lu[b]

This article proposes a dual-band terahertz multi-functional absorber based on graphene and indium antimonide (InSb), which can be electrically, thermally, and magnetically tuned. The results indicate that, in the absence of an external magnetic field, the absorber exhibits two distinct absorption peaks based on the bright–bright mode coupling of cross-shaped and circular InSb arrays, with an average absorption rate of 99.8%. Meanwhile, its physical absorption mechanism can be theoretically analyzed by the radiating two-oscillator (RTO) model and the distribution of electric field at absorption peaks. Secondly, when the external magnetic field is applied along the *X* direction, the absorption frequency and absorption rate of the absorber can be electrically tuned by changing the chemical potential of graphene, and thermally and magnetically controlled by changing the temperature of InSb and the magnitude of the external magnetic field. Afterwards, the effects of the length and width of the cross-shaped InSb array, the radius of the InSb circle, and the thickness of the dielectric layer on the absorption effect are discussed. Finally, further studies are conducted on the application prospects of the absorber as a refractive index sensor, temperature sensor, and magnetic field sensor. This work provides a theoretical basis for the design of multi-tuned absorbers and sensors.

Received 27th December 2025
Accepted 10th March 2026

DOI: 10.1039/d5ra10034h

rsc.li/rsc-advances

Introduction

In recent years, terahertz waves have attracted significant attention from the academic community due to their widespread applications in wireless communication,[1] electron devices,[2] 6G application,[3] antenna,[4] magnetic shields,[5] and quantum mechanical treatments.[6,7] Meanwhile, terahertz absorbers also have broad application prospects in electromagnetic absorption,[8] biosensing,[9] and energy harvesting.[10] However, for terahertz absorbers based on traditional materials, once their geometric parameters are determined, their absorption performance is difficult to control, which severely limits their practical applications.

With the continuous deepening of research, various tunable metamaterial absorbers have been developed based on Dirac semimetals (BDS),[11–14] graphene,[15–18] vanadium dioxide (VO_2),[19–22] strontium titanate (STO),[23–25] and indium antimonide (InSb)[26–28] to achieve dynamic tuning characteristics. Among them, graphene has many unique properties, such as dynamic tunability, strong localization, and tight field confinement. InSb, as a thermal and magnetostatic phase change material, can undergo a state transition from isotropic to anisotropic under the influence of an external magnetic field. Therefore, Zhou *et al.* proposed a dynamically tunable metasurface, which enables radiative cooling, light detection and infrared camouflage.[29] Li *et al.* delved into a ground-to-unmanned aerial vehicle (UAV) channel at 140 GHz, with a specific focus on the influence of UAV hovering behavior on channel performance.[30] Meng *et al.* proposed a framework for widely linear beamforming in a coprime array with non-uniform noise.[31] Zhang *et al.* designed an explainable and trust-aware AI-driven network slicing framework for 6G IoT using deep learning.[32] In addition, Jing *et al.* designed a thermally and magnetically tunable terahertz absorber based on InSb.[33] However, so far, the research on electrically, thermally, and magnetically triple-tunable metamaterial absorbers based on graphene and InSb has not been reported in public literature.

Therefore, this paper proposes a dual-band terahertz multifunctional triple-tunable absorber based on graphene and InSb. Firstly, based on the bright–bright mode coupling effect of cross shaped and circular InSb arrays, two distinct absorption peaks appear in the absorption spectrum of the absorber at 0.4482 THz and 1.1211 THz, with absorption rates of 99.6% and 99.9%, respectively. Secondly, the absorption mechanism can be theoretically analyzed through the radiating two-oscillator (RTO) model and the distribution of electric field at absorption peaks. Thirdly, by precisely adjusting the chemical potential of graphene, the temperature of InSb, and the magnitude of the external magnetic field, the absorption frequency and absorption rate of the absorber can be electrically, thermally, and

[a]*College of Science, Yunnan Agricultural University, Kunming, 650201, China. E-mail: hubaojing@ynau.edu.cn*
[b]*College of Big Data, Yunnan Agricultural University, Kunming, 650201, China*

magnetically tuned. Afterwards, the variations of the absorption spectra of absorber with the parameters are discussed in detail. Finally, the possible uses of double-band absorber as refractive index sensor, temperature sensor, and magnetic field sensor are further discussed. This work provides potential basis for the design of triple-tunable absorbers and sensors.

Materials

The surface conductivity of graphene can be expressed as $\sigma_{graphene} = \sigma_{intra} + \sigma_{inter}$. The intraband and interband contributions can be calculated as follow:[34,35]

$$\sigma_{intra}(\omega, \mu_c, \Gamma, T) = \frac{je^2}{\pi\hbar^2(\omega - j2\Gamma)} \int_0^\infty \left(\frac{\partial f_d(E, \mu_c, T)}{\partial E} - \frac{\partial f_d(-E, \mu_c, T)}{\partial E} \right) E \, dE \quad (1)$$

$$\sigma_{inter}(\omega, \mu_c, \Gamma, T) = \frac{je^2(\omega - j2\Gamma)}{\pi\hbar^2} \int_0^\infty \left(\frac{f_d(E, \mu_c, T) - f_d(-E, \mu_c, T)}{(\omega - j2\Gamma)^2 - 4E/\hbar^2} \right) dE \quad (2)$$

here, $f_d(E, \mu_c, T) = (e^{(E-\mu_c/K_BT)} + 1)^{-1}$ is the Fermi Dirac distribution function. ω is the angular frequency of the incident light. K_B and $\hbar$ represent the Boltzmann constant and reduced Planck constant, respectively. e is the charge number of an electron. The absolute temperature of the environment is set as T. μ_c represents chemical potential of graphene. E is the energy, and $\Gamma = 2\tau^{-1}$ is the phenomenological scattering rate. The electron-phonon relaxation time is denoted as τ which will be set as $\tau =$ 0.025 ps in the following calculation.[36]

On the other hand, InSb can be regarded as an isotropic medium, and its dielectric constant can be represented by the Drude model, when the external magnetic field is absent:[37]

$$\varepsilon_{InSb} = \varepsilon_\infty - \frac{{\omega_p}^2}{\omega^2 + j\omega\gamma_0} \quad (3)$$

Among them, $\varepsilon_\infty = 15.68$, and $\gamma_0 = \pi \times 10^{11}$ rad s^{-1} represents damping constants. Furthermore, ${\omega_p}^2 = Ne^2/\varepsilon_0 m^*$ represents the bulk plasma frequency. $m^* = 0.015m_e$ is the effective mass of free charge carriers. $m_e = 9.109 \times 10^{-31}$ kg indicates electronic mass, and N represents the carrier concentration, which can be expressed as:

$$N = 5.76 \times 10^{20} T^{3/2} \exp\left(\frac{-E_g}{2K_BT}\right) \quad (4)$$

where T is the external temperature, and $E_g = 0.26$ eV represents the band-gap energy.

In addition, as mentioned in the introduction, if an external magnetic field is applied along X direction, the state of InSb will change from isotropic to anisotropic, and the dielectric constant of InSb can be expressed as a tensor $\varepsilon(\omega)$:[38]

$$\varepsilon(\omega) = \begin{bmatrix} \varepsilon_{xx} & 0 & 0 \\ 0 & \varepsilon_{yy} & \varepsilon_{yz} \\ 0 & -\varepsilon_{yz} & \varepsilon_{zz} \end{bmatrix} \quad (5)$$

$$\varepsilon_{xx} = \varepsilon_\infty - \frac{{\omega_p}^2}{\omega^2 + j\omega\gamma_0} \quad (6)$$

$$\varepsilon_{yy} = \varepsilon_{zz} = \varepsilon_\infty - \frac{{\omega_p}^2(\omega^2 + j\omega\gamma_0)}{(\omega^2 + j\omega\gamma_0)^2 - (\omega^2{\omega_c}^2)} \quad (7)$$

$$\varepsilon_{yz} = \frac{j\omega\omega_c{\omega_p}^2}{(\omega^2 + j\omega\gamma_0)^2 - \omega^2{\omega_c}^2} \quad (8)$$

$$\omega_c = eB/m^* \quad (9)$$

The cyclotron frequency ω_c is related to the applied magnetic field B. Therefore, the dielectric constant of InSb can also be adjusted by changing the magnitude of the applied magnetic field.

Fig. 1 shows the variations of the InSb dielectric constant under different temperatures when the external magnetic field is absent. As shown in Fig. 1, with the increase of external temperature, the real parts of InSb dielectric constant gradually decrease and the imaginary parts gradually increase. In addition, as the temperature changes, the real parts of the dielectric constant of InSb are negative, indicating that InSb has metallic properties in this frequency range.

Radiating two-oscillator (RTO) model

The absorption mechanism based on the bright–bright mode coupling effect can be theoretically analyzed by using the radiation two-oscillator (RTO) model.[39–41]

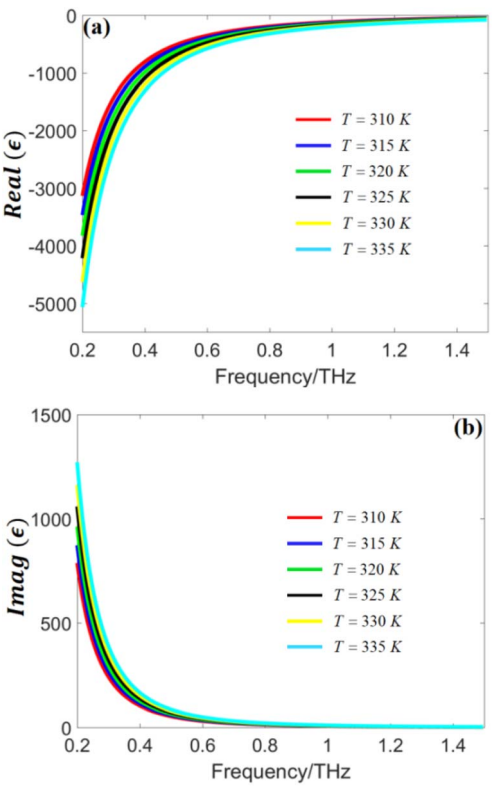

Fig. 1 The (a) real parts and (b) imaginary parts of dielectric constant for InSb with different temperatures.

$$\ddot{p_1}(t) + \gamma_1 \dot{p_1}(t) + \omega_1^2 p_1(t) - \Omega^2 \exp(j\phi) p_2(t) = f_1(t) \quad (10)$$

$$\ddot{p_2}(t) + \gamma_2 \dot{p_2}(t) + \omega_2^2 p_2(t) - \Omega^2 \exp(j\phi) p_1(t) = f_2(t) \quad (11)$$

here, the first and second bright mode resonators are denoted as $p_1(t)$ and $p_2(t)$, respectively. ω_1 is the resonant frequency of $p_1(t)$, and ω_2 is the resonant frequency of $p_2(t)$. The damping factor of $p_1(t)$ is denoted as γ_1, and the damping factor of $p_2(t)$ is denoted as γ_2. $\Omega^2 \exp(j\phi)$ is the complex coupling coefficient, ϕ is the phase shift between two resonant modes. In subsequent calculations, we can assume that the external forces $f_1(t) = f_2(t)$ and phase shifts $\phi = 0$, because both bright mode units are illuminated by the same incident light.

By assuming $p_1(t) = p_1 \exp(-j\omega t)$, $p_2(t) = p_2 \exp(-j\omega t)$ and $f_1(t) = f_2(t) = f \exp(-j\omega t)$, in the frequency domain, eqn (10) and (11) can be solved as follows:

$$P_1 = \frac{\Omega^2 + (\omega_2^2 - \omega^2 - j\omega\gamma_2)}{(\omega_1^2 - \omega^2 - j\omega\gamma_1)(\omega_2^2 - \omega^2 - j\omega\gamma_2) - \Omega^4} f \quad (12)$$

$$P_2 = \frac{\Omega^2 + (\omega_1^2 - \omega^2 - j\omega\gamma_1)}{(\omega_1^2 - \omega^2 - j\omega\gamma_1)(\omega_2^2 - \omega^2 - j\omega\gamma_2) - \Omega^4} f \quad (13)$$

Furthermore, the relationship between surface conductivity σ_e and current density J in thin structure can be described as:

$$J = -jn_s\omega(P_1 + P_2) = \sigma_e E_s \quad (14)$$

Among them, n_s represents the average electron density. E_s is the spatial average electric field on the current sheet. Under the approximate conditions of $f \propto E_s$, the surface conductivity σ_e can be solved by the following equation:

$$\sigma_e = -jn_s\omega \frac{2\Omega^2 + (\omega_2^2 - \omega^2 - j\omega\gamma_2) + (\omega_1^2 - \omega^2 - j\omega\gamma_1)}{(\omega_1^2 - \omega^2 - j\omega\gamma_1)(\omega_2^2 - \omega^2 - j\omega\gamma_2) - \Omega^4} \quad (15)$$

When the σ_e is determined, the reflection and transmission coefficients of metamaterial can be expressed as:

$$R = \frac{-Z_0\sigma_e}{2 + Z_0\sigma_e} \quad (16)$$

$$T = \frac{2}{2 + Z_0\sigma_e} \quad (17)$$

here, Z_0 is the wave impedance of incident light. Finally, the reflectivity and transmissivity of the metamaterial absorber can be obtained by fitting the corresponding $|R|^2$ and $|T|^2$, and the absorptivity can be derived from $A = 1 - |R|^2 - |T|^2$. Specifically, if the transmissivity of absorber is zero, the absorptivity can be calculated as $A = 1 - |R|^2$.[42]

Theoretical model of triple-tunable dual-band absorber

Fig. 2 shows the model diagram of triple-tunable dual-band absorber. The model consists of six layers: the top layer is InSb thin film layer with a composite structure of cross shaped and circular InSb arrays, which are used to achieve the dual-band absorption effect and thermal and magnetic dual-tuning characteristics. The length and width of the cross shaped InSb film is $L = 60$ μm and $w = 16$ μm respectively. The radius of the circular InSb film is $R_0 = 10$ μm. The thickness of them are $h_1 = 0.2$ μm. The dielectric layer is Teflon layer. Its thickness and dielectric constant are $h_2 = 60$ μm and $\varepsilon_{Teflon} = 2.1$, respectively. The bottom layer is a copper substrate layer with a thickness of $h_3 = 0.2$ μm and a conductivity of $\sigma = 5.8 \times 10^7$ S m^{-1}. The period of the model is $p_x = p_y = 80$ μm.

Graphene, as a 2D material, is located between the InSb and Teflon layers to achieve the electrically controlled characteristics of the absorber. In addition, the Topas film is used as an insulating spacer to connect graphene and InSb layers, and the polysilicon layer can be used as an electrode to control the chemical potential of graphene. The polysilicon and Topas layers have almost no effect on the absorption performance because their thicknesses are only 20 nm.

The incident light propagates in the $-Z$ direction, and the polarization is in the X direction. The numerical simulations are conducted by utilizing the CST Microwave Studio. Also, the simulation is carried out with 20 cells per wavelength, and launching the adaptive meshing. The meshes are adjusted numerous times to ensure obtaining consistent results. We set the unit cell boundary conditions on both the x- and y-axes, and the perfect matching layer on the z-axis, toward which the electromagnetic wave propagates. At first, the applied magnetic field is absent. Afterwards, the applied magnetic field is along the X axis.

Discussion on the results of triple-tunable dual-band absorber

Fig. 3(a) shows the transmittance, reflectance, and absorptance curves of the triple-tunable dual-band absorber when the chemical potential of graphene is $\mu_c = 0$ eV and the temperature of InSb is $T = 330$ K.

Firstly, it can be seen from Fig. 3(a) that the absorptivity of the absorber reaches 99.6% and 99.9% at 0.4482 THz and 1.1211 THz, respectively. The average absorptivity of the two absorption peaks is 99.8%, achieving the perfect absorption. Meanwhile, since the thickness of the copper substrate layer is larger than the skin depth in the terahertz band, the transmittance of the dual-band model is always zero within the analyzed frequency range.

Secondly, as shown in Fig. 3(b), both the cross shaped and circular InSb arrays exhibit Lorentzian line-shaped resonance, indicating that they can be regarded as bright mode units that can directly interact with incident light. At the same time, the absorption frequencies of the cross-shaped and circular InSb arrays are approximately equal to those at peak A and peak B. Therefore, the dual-band absorption effect can be explained as the result of bright–bright mode coupling between the cross-shaped and circular InSb arrays.[43,44]

Thirdly, as mentioned in introduction, the absorption effect resulted from bright–bright mode coupling can theoretically be explained by using the RTO model. Hence, as shown in Fig. 3(c), under different L and R_0, the theoretical results of the RTO model are consistent with the CST numerical simulation results, which also confirms that the dual-band absorption

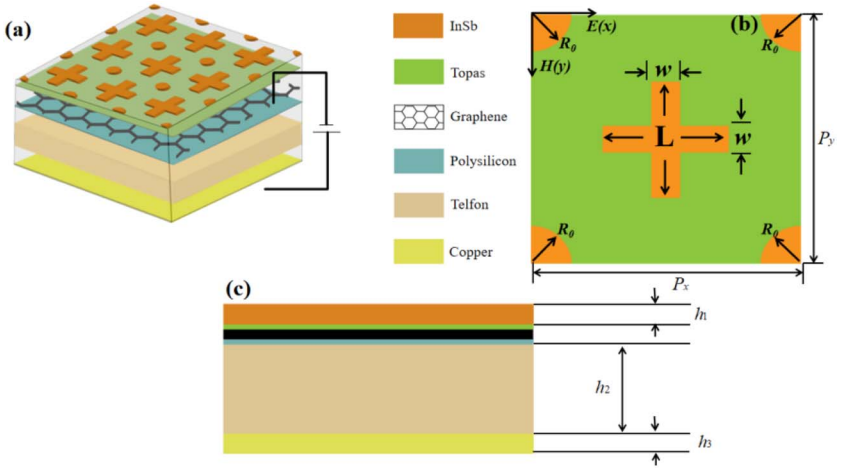

Fig. 2 Model diagrams of the triple-tunable double-band absorber: (a) 3D view, (b) top view, and (c) side view.

effect is generated by the bright–bright mode coupling between the crossed shaped and circular InSb arrays. The fitting procedures are as follows: first, the formula for absorptance as a function of ω_1, ω_2, γ_1, γ_2, n_sZ_0, and Ω^2 is derived in RTO model. Then, the formula is used to fit the simulated data of absorptance in Fig. 3(c) by using the software 1stopt, from which the fitting curve of the RTO model can be obtained. The fitting parameters of $L = 60$ μm, $R_a = 10$ μm are shown in Table 1.

Finally, Fig. 3(d) shows the absorption spectra of the dual-band model at different polarization angles. Due to the symmetric characteristic of the model, when the polarization angle increases from $\theta = 0°$ to $\theta = 90°$, the absorption frequencies and absorption rates at peaks A and B remain basically unchanged, exhibiting the polarization-independent characteristic.

Fig. 4 shows the electric field intensity distributions of dual-band model at peaks A and B under *X*-polarized light and *Y*-polarized light, respectively. Both the electric field intensity distributions are analyzed in the *X*–*Y* plane.

Firstly, in Fig. 4(a), when the incident light is *X*-polarized, at 0.4482 THz (peak A), the electric field is mainly distributed near the cross-shaped InSb film and exhibits a typical dipole mode distribution. However, in Fig. 4(b), at 1.1211 THz (peak B), the electric field spreads on the vicinity of both cross-shaped InSb and circular InSb films, also showing a typical dipole mode distribution.

Secondly, in Fig. 4(c) and (d), when the incident light is *Y*-polarized, the electric fields in the *X*–*Y* plane are perpendicular to those in Fig. 4(a) and (b), respectively, but the electric field distributions are approximately consistent, due to the symmetry of the model.[32]

The absorption effect of the dual-band absorber proposed in this paper can be considered as being generated by the excitation of the LC resonance mode, with the resonant frequency of $f_1 = 1/2\pi\sqrt{L_1C_1}$. On the other hand, both the equivalent capacitance C_1 and equivalent inductance L_1 are affected by the model parameters. Therefore, Fig. 5 shows the changes in the absorption spectra of the dual-band absorber under different parameters.

In Fig. 5(a), as the length of cross-shaped InSb array L increases, the absorption frequencies at peak A gradually decrease, undergoing a red shift, due to an increase in the equivalent inducance L_1.[33] Meanwhile, the absorption rates at peak A first increase and then decrease. Besides, as the L increases, its absorption rates at peak B increase continuously, while the absorption frequencies at that remain basically unchanged.

In Fig. 5(b), as the width of cross-shaped InSb array w increases, the absorption frequencies at peak A gradually increase, experiencing a blue shift, due to the equivalent capacitance C_1 decreases.[33] The absorption rates at that also gradually increases. Additionally, at peak B, as w increases, the absorption frequencies remain basically unchanged, and the absorption rates gradually increase.

In Fig. 5(c), as the radius of the InSb circle R_0 increases, the absorption frequencies at peak B gradually decrease, while the absorption rates increase slowly. Meanwhile, as R_0 changes, the absorption frequencies and absorption rates at peak A remain basically unchanged.

Due to the InSb layer, Teflon layer, and copper substrate layer construct an equivalent Fabry–Perot (F–P) resonator. The thickness of the Teflon layer h_2 has significant influences on the interaction between the InSb layer and incident wave. Therefore, in Fig. 5(d), when the thickness of the h_2 increases, the absorption rates at peaks A and B first increase and then decrease, with a more significant change at peak B, compared to peak A. When the $h_2 = 60$ μm, the absorption rates at the two absorption peaks reached its maximum value. Furthermore, as h_2 increases, the absorption frequencies at peak A and peak B remain approximately constant.

Fig. 6 analyzes the application prospects of the dual-band absorber as a refractive index sensor. As the refractive index of the surrounding medium increases, the effective permittivity of the model increases accordingly. Meanwhile, according to the perturbation theory,[45] when the permittivity increases, the

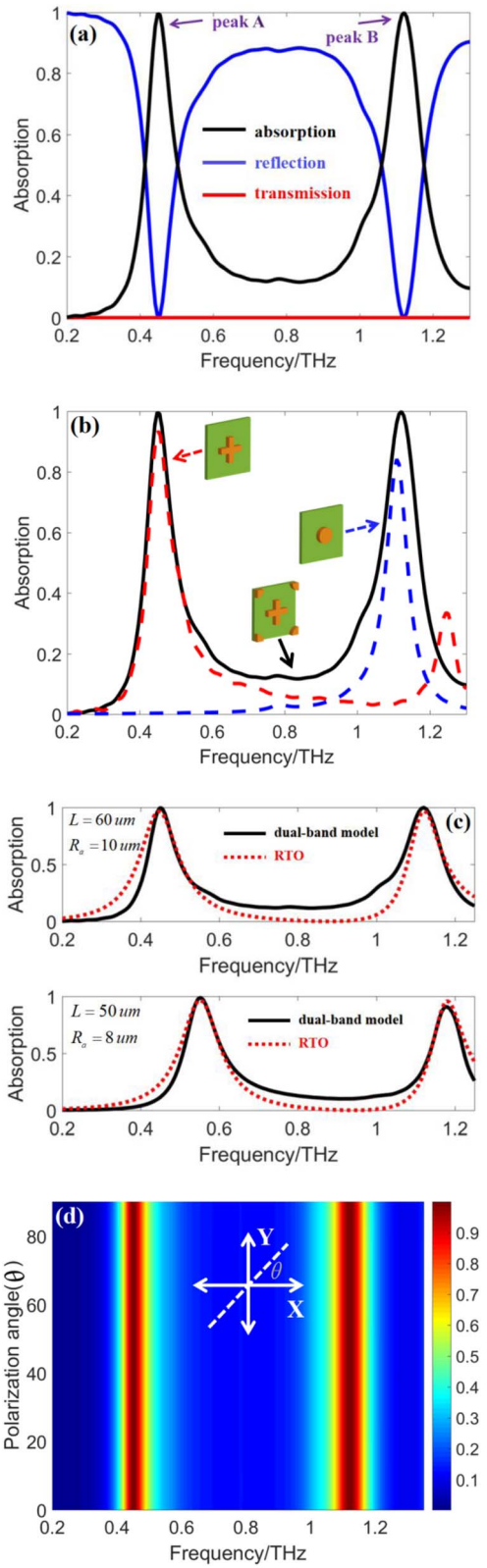

Fig. 3 (a) The transmittance, reflectance, and absorption rate curves of double-band absorber model, (b) the relationships between the absorption spectra of cross-shaped, circular InSb arrays, and dual-band model, (c) the comparison between CST simulations and RTO results; (d) the variation law of absorption spectra under different polarization angles.

Table 1 The fitting parameters of RTO model

ω_1 (THz)	ω_2 (THz)	γ_1 (THz)	γ_2 (THz)	$n_s Z_0$ (THz)	Ω^2 (THz)
0.4482	1.1211	0.001	0.001	0.226	0.04

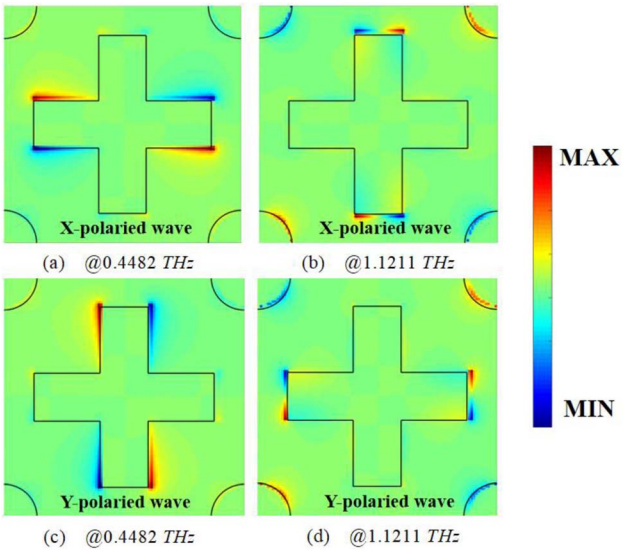

Fig. 4 Electric field distributions under: (a) *X*-polarized wave at peak A, (b) *X*-polarized wave at peak B, (c) *Y*-polarized wave at peak A, and (d) *Y*-polarized wave at peak B.

resonant frequency of the absorber will decrease. Therefore, in Fig. 6(a), as the background refractive index increases, the absorption frequencies at peaks A and B show obvious red shift. At the same time, the absorption rates at peak A decrease slowly, while the absorption rates at peak B remain approximately constant.

In addition, in Fig. 6(b), when the refractive index increases from $n = 1.0$ to $n = 1.5$, the changes in the absorption frequencies at peaks A and B show an approximately linear relationship with the changes in the refractive index. By calculating the sensitivity $S = \Delta f/\Delta n$. We conclude that the sensitivity of peak A is $S = 130.6$ GHz per RIU and that of peak B is $S = 378.8$ GHz per RIU, demonstrating excellent refractive index sensing performance. The comparison of sensing performance between different metamaterial absorbers is shown in Table 2.

Electrically, thermally and magnetically tunable characteristics

To verify the electrically, thermally, and magnetically triple-tunable performances of dual-band absorber, Fig. 7 shows the variations of the absorption spectra with different graphene chemical potential, InSb temperature, and external magnetic field magnitude.

Fig. 7(a) shows the variation trends of the absorption spectra under different chemical potential of graphene. As shown in the Fig. 7(a), when the chemical potential changes from $\mu_c = 0$ eV to $\mu_c = 0.4$ eV, the absorption rates at peak A decrease from 0.9961

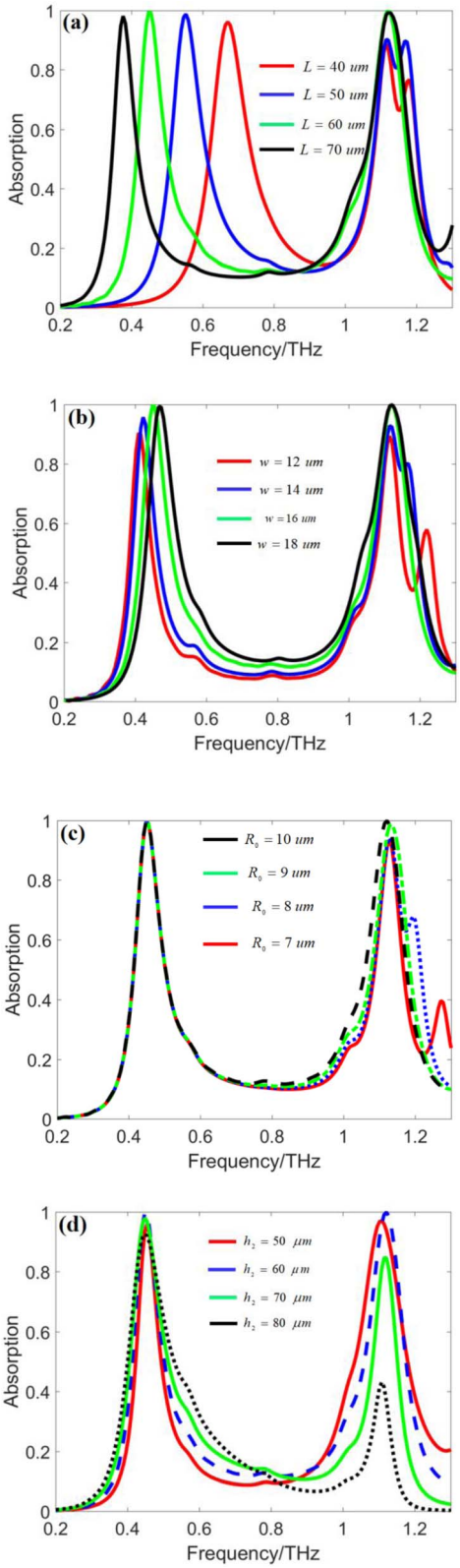

Fig. 5 The variation trends of absorber model with respect to (a) length of cross-shaped InSb array; (b) width of cross-shaped InSb array; (c) circular radius of InSb circle; (d) thickness of Teflon layer.

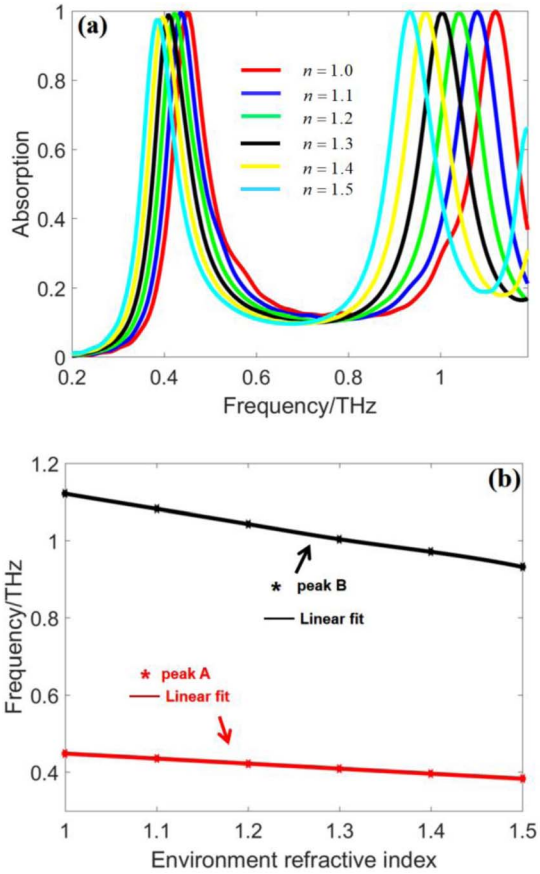

Fig. 6 The variation trends of (a) absorption spectra, (b) absorption frequencies with different refractive indices.

Table 2 The comparison on sensing performance

References	Refractive index	Sensitivity
46	1.0–1.4	300 GHz per RIU
47	1.0–1.8	360 GHz per RIU
48	1.1–1.9	187 GHz per RIU
Paper	1.0–1.5	378.8 GHz per RIU

to 0.6063, and that at peak B decrease from 0.9992 to 0.6491. In addition, the absorption frequencies at peak B decrease from 1.1211 THz to 1.0493 THz, while that at peak A remain almost unchanged.

As shown in Fig. 1(a), when the temperature of InSb increases, the real part of its dielectric constant gradually decreases. Therefore, in Fig. 7(b), when the temperature of InSb increases, the absorption frequencies at peak A change from 0.4156 THz to 0.4678 THz, and that at peak B vary from 1.0166 THz to 1.1734 THz. Meanwhile, as the temperature increases, the absorption rates at peak A gradually increase from 96.1% to 99.5%, while the rate at peak B remains almost unchanged. When $T = 330$ K, the average absorption rate at the two absorption peaks reaches the maximum value.

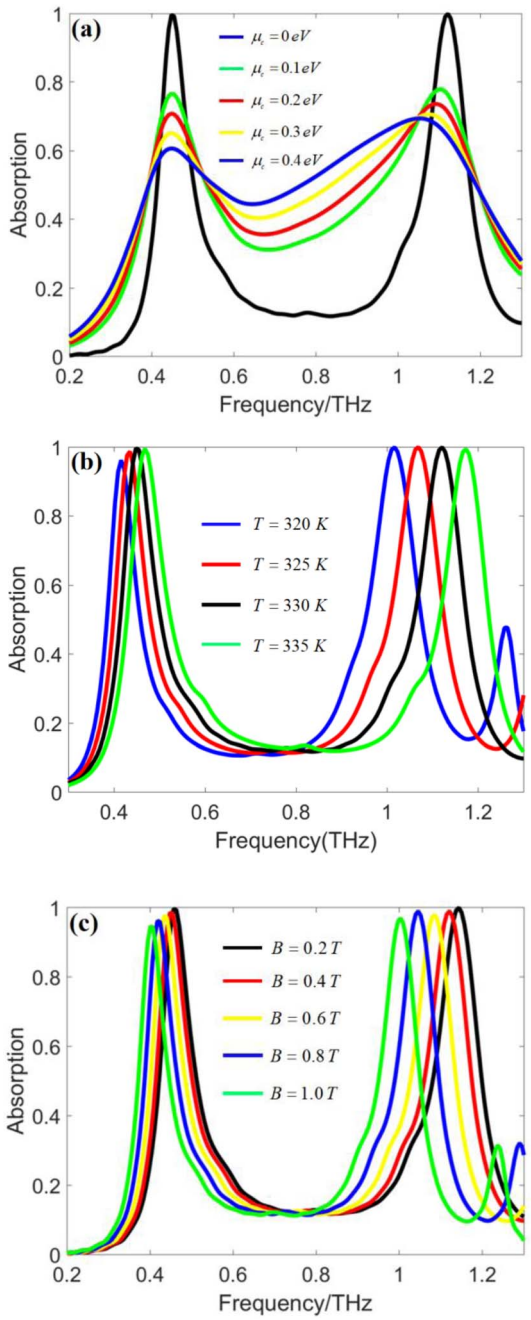

Fig. 7 Variation trends of absorption spectra with different (a) graphene chemical potential, (b) InSb temperature, (c) magnitude of applied magnetic field.

According to formulas (5)–(9), if external magnetic field is applied, the state of InSb will change from isotropic to anisotropic, and the dielectric constant of InSb can be adjusted by changing the magnitude of the applied magnetic field. Therefore, in Fig. 7(c), when the magnitude of the external magnetic field increases from $B = 0.2$ T to $B = 1.0$ T, the absorption frequencies at peaks A and B gradually decrease, resulting in red shift. Meanwhile, the absorption rates at peak A gradually decrease, and that at peak B remain approximately unchanged.

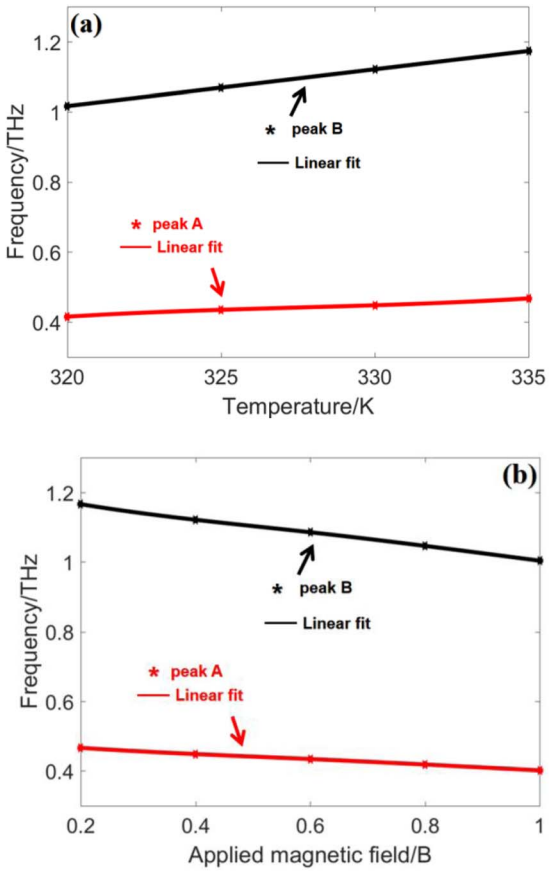

Fig. 8 Variation trends of absorption frequencies at (a) different temperatures, (b) different magnetic fields.

Finally, Fig. (8) analyzes the application prospects of the dual-band absorber as temperature and magnetic field sensors. As shown in the Fig. 8, when the InSb temperature and the magnitude of the external magnetic field change, the changes in the absorption frequencies at peaks A and B also show an approximately linear relationship with the changes in the external temperature and magnetic field.

In Fig. 8(a), the temperature sensing sensitivity of the absorber can reach $S = 10.45$ GHz K^{-1}. In Fig. 8(b), the magnetic field sensing sensitivity of the absorber can reach $S = 203.2$ GHz T^{-1}. It also demonstrates good temperature and magnetic field sensing performance.

Conclusion

This paper proposes a dual-band terahertz multi-functional absorber based on graphene and InSb that can be electrically, thermally, and magnetically tuned. Firstly, the absorber exhibits two distinct absorption peaks at 0.4482 THz and 1.1211 THz, with an average absorption rate of 99.8%. Secondly, by analyzing the correlation between the absorption spectra of the cross-shaped InSb array, the circular InSb array, and the dual-band model, the high absorption mechanism can be ascribed to the bright–bright-mode coupling effect between the two InSb arrays. Furthermore, this mechanism is theoretically confirmed

by the RTO model and the electric field distribution at the two absorption peaks. Thirdly, when the graphene chemical potential, InSb temperature, and external magnetic field change, the absorption rate and absorption frequency at the absorption peaks can be dynamically changed accordingly. Finally, it can be found that when the model is used as refractive index sensor, temperature sensor, and magnetic field sensor, its sensitivities can reach 378.8 GHz per RIU, 10.45 GHz K^{-1}, and 203.2 GHz T^{-1} respectively. This work provides potential basis for the design of triple-tunable absorbers and sensors.

Author contributions

The authors have contributed to this article in the following way: Baojing Hu and Changjin Cai designed the triple-tunable dual-band terahertz metamaterial absorber. Ke Li and Weifeng Lu made the simulation. Baojing Hu and Changjin Cai wrote the main manuscript text. All authors reviewed the manuscript.

Conflicts of interest

The authors declare that they have no conflicts of interest or competing interests.

Data availability

All the data generated during and/or analyzed during the current study are available from the corresponding author upon reasonable request.

Acknowledgements

This work was supported by the National Natural Science Foundation of China (62363035), and Yunnan Province Basic Research Project (202301AT070495).

Notes and references

1 L. Liu, F. Wang and X. Yin, Low-Loss Flexible Filter Based on Compact Double Interdigital Coupling SIR With TPV Technology for Bendable Wireless Communications, *IEEE Microw. Wirel. Technol. Lett.*, 2025, **1**, 1–4.
2 F. Wang, C. Sun and X. Yin, Investigation on Electromigration Failure Mechanism and Lifetime Prediction of Interconnects Under Multifield Coupling for Chiplet Applications, *IEEE Trans. Electron. Dev.*, 2025, **73**, 552–560.
3 N. Zhu, Y. Zhang and Z. Zhao, Design of a Compact Wideband SPDT Switch With High Isolation for Sub-6 GHz Applications, *IEEE Trans. Circuits Syst., II Express Briefs*, 2025, **73**, 43–47.
4 L. Gai, Y. Xu and P. Liu, Design of a Spatial Multi-Mode Energy Selective Antenna Integrating Electromagnetic Protection and Anti-Interference Capabilities, *IEEE Trans. Antenn. Propag.*, 2026, **1**, 1.
5 Y. Dou, Y. Gao and K. Wang, Analysis and measurement of shielding performance in large-scale HTS magnetic shields under ultralow magnetic fields, *Measurement*, 2026, **259**, 119636.
6 J. M. Lao, K. X. Guo and J. Y. Lan, Influence of terahertz field on optical absorption coefficients and refractive index changes in double semi-V-shaped quantum wells, *J. Opt. Soc. Am. B*, 2020, **37**, 2308–2313.
7 A. Alnaghmaish, H. Dakhlaoui and T. Ghrib, Effects of magnetic, electric, and intense laser fields on the optical properties of AlGaAs/GaAs quantum wells for terahertz photodetectors, *Phys. B*, 2022, **635**, 413838.
8 M. Diem, T. Koschny and C. M. Soukoulis, Wide-angle perfect absorber/thermal emitter in the terahertz regime, *Phys. Rev. B*, 2009, **79**, 033101.
9 D. Cheng, X. He and B. Huang, Terahertz biosensing metamaterial absorber for virus detection based on spoof surface plasmon polaritons, *Int. J. RF Microw. Computer-Aided Eng.*, 2018, **28**, e21448.
10 H. Wang, V. Prasad Sivan and A. Mitchel, Highly efficient selective metamaterial absorber for high-temperature solar thermal energy harvesting, *Sol. Energy Mater. Sol. Cell.*, 2015, **137**, 235–242.
11 Y. Zhang, J. Lv and L. Que, A double-band tunable perfect terahertz metamaterial absorber based on Dirac semimetals, *Results Phys.*, 2019, **15**, 102773.
12 W. Meng, L. Que and J. Lv, A triple-band terahertz metamaterial absorber based on buck Dirac semimetals, *Results Phys.*, 2019, **14**, 102461.
13 G. D. Liu, X. Zhai and H. Y. Meng, Dirac semimetals based tunable narrowband absorber at terahertz frequencies, *Opt. Express*, 2018, **26**, 11471–11480.
14 P. Fang, X. Shi and C. Liu, Single- and dual-band convertible terahertz absorber based on bulk Dirac semimetal, *Opt. Commun.*, 2020, **462**, 125333.
15 Z. Liu, Z. Zhang and F. Zhou, Dynamically tunable electro-optic switch and multimode filter based on twisted bilayer graphene strips, *J. Opt.*, 2021, **23**, 025104.
16 H. Cheng, S. Chen and P. Yu, Dynamically tunable plasmonically induced transparency in periodically patterned graphene nanostrips, *Appl. Phys. Lett.*, 2013, **103**, 203112.
17 F. Zhou, Y. Wang and X. Zhang, Dynamically adjustable plasmon-induced transparency and switching application based on bilayer graphene metamaterials, *J. Phys. D Appl. Phys.*, 2021, **54**, 054002.
18 A. Lherbier, B. Biel and Y.-M. Niquet, Transport Length Scales in Disordered Graphene-Based Materials: Strong Localization Regimes and Dimensionality Effects, *Phys. Rev. Lett.*, 2008, **100**, 036803.
19 J. R. Liang, M. J. Wu and M. Hu, Fabrication of VO_2 thin film by rapid thermal annealing in oxygen atmosphere and its metal—insulator phase transition properties, *Chin. Phys. B*, 2014, **23**, 076801.
20 Y. N. Liu, X. L. Weng and P. Zhang, Ultra-Broadband Infrared Metamaterial Absorber for Passive Radiative Cooling, *Chin. Phys. Lett.*, 2021, **38**, 034201.

21 M. T. Nouman, J. H. Hwang and M. Faiyaz, Vanadium dioxide based frequency tunable metasurface filters for realizing reconfigurable terahertz optical phase and polarization control, *Opt. Mater.*, 2018, **26**, 12922–12929.
22 J. K. Wahlstrand and E. J. Heilweil, Contactless THz-based bulk semiconductor mobility measurements using two-photon excitation, *Opt. Express*, 2018, **26**, 29848–29853.
23 Y. Zhao, B. Li and C. Lan, Tunable silicon-based all-dielectric metamaterials with strontium titanate thin film in terahertz range, *Opt. Express*, 2017, **25**, 22158–22163.
24 X. Huang, W. He and F. Yang, Thermally tunable metamaterial absorber based on strontium titanate in the terahertz regime, *Opt. Mater. Express*, 2019, **9**, 1377–1385.
25 J. Leng, J. Peng and G. Wang, Investigation of strontium titanate spherical shell supported terahertz all-dielectric metamaterials, *J. Opt. Soc. Am. B*, 2021, **38**, 3466–3473.
26 P. Kumar, A. Lakhtakia and P. K. Jain, Tricontrollable pixelated metasurface for absorbing terahertz radiation, *Appl. Opt.*, 2019, **58**, 9614–9623.
27 Y. Liang, S. Pakniyat and Y. Xiang, Temperature-dependent transverse-field magneto-plasmons properties in InSb, *Opt. Mater.*, 2021, **112**, 110831.
28 H. Li, W. Huang and W. Zhang, Thermally controlled electromagnetically induced transparency in hybrid metal-InSb metamaterials at THz frequencies, *J. Phys., Conf. Ser.*, 2020, **1592**, 012024.
29 G. Zhou, J. Huang and H. Li, Multispectral camouflage and radiative cooling using dynamically tunable metasurface, *Opt. Express*, 2024, **32**, 12026–12940.
30 D. Li, P. Li and J. B. Zhao, Ground-to-UAV sub-terahertz channel measurement and modeling, *Opt. Express*, 2024, **32**, 32482–32494.
31 Z. Meng, F. Shen and S. Gazor, WLB-CANUN: Widely Linear Beamforming in Coprime Array with Non-Uniform Noise, *IEEE Trans. Veh. Technol.*, 2024, **74**, 5833–5842.
32 K. Zhang, B. Zheng and J. Xue, Explainable and Trust-Aware AI-Driven Network Slicing Framework for 6G IoT Using Deep Learning, *IEEE Internet Things J.*, 2025, **1**, 1.
33 H. Jing, Y. Wei and J. Duan, Thermally and magnetically controlled dual-band terahertz metamaterial absorber based on InSb, *Opt. Mater.*, 2022, **129**, 112311.
34 L. Ye, X. Chen and C. Zhu, Switchable broadband terahertz spatial modulators based on patterned graphene and vanadium dioxide, *Opt. Express*, 2020, **28**, 33948–33958.
35 A. Vakil and N. Engheta, Transformation Optics Using Graphene, *Science*, 2011, **332**, 1291–1294.
36 Y. Liu, R. Zhong and Z. Lian, Dynamically tunable band stop filter enabled by the metal-graphene metamaterials, *Sci. Rep.*, 2018, **8**, 2828.
37 M. Ziaee Bideskan, K. Forooraghi and Z. Atlasbaf, Method of lines for analysis of plane wave scattering by periodic arrays of magnetically-biased graphene strips, *Sci. Rep.*, 2021, **11**, 7588.
38 J. Han, A. Lakhtakia and C. W. Qiu, Terahertz metamaterials with semiconductor split-ring resonators for magnetostatic tunability, *Opt. Express*, 2008, **16**, 14390–14396.
39 X. Hu, S. Yuan and A. Armghan, Plasmon induced transparency and absorption in bright–bright mode coupling metamaterials: a radiating two-oscillator model analysis, *J. Phys. D Appl. Phys.*, 2017, **50**, 025301.
40 P. Tassin, T. Koschny and C. M. Soukoulis, Effective material parameter retrieval for thin sheets: Theory and application to graphene, thin silver films, and single-layer metamaterials, *Phys. B*, 2012, **407**, 4062–4065.
41 P. Tassin, L. Zhang and R. Zhao, Electromagnetically Induced Transparency and Absorption in Metamaterials: The Radiating Two-Oscillator Model and Its Experimental Confirmation, *Phys. Rev. Lett.*, 2012, **109**, 187401.
42 B. J. Hu, M. Huang and L. Yang, Dual-controlled tunable absorber using a hybrid Dirac semimetal–strontium titanate metamaterial, *J. Opt. Soc. Am. B*, 2023, **40**, 688–694.
43 B. J. Hu, M. Huang and P. Li, Dynamically dual-tunable dual-band to four-band metamaterial absorbers based on bulk Dirac semimetal and vanadium dioxide, *J. Opt. Soc. Am. A*, 2022, **39**, 383–391.
44 B. J. Hu, M. Huang and H. W. Ding, Dual-tunable triple-band absorber based on bulk Dirac semimetal and vanadium dioxide, *J. Infrared Millimeter Waves*, 2023, **42**, 215–222.
45 J. Hwang and J. W. Roh, Electrically tunable two-dimensional metasurfaces at near-infrared wavelengths, *Opt. Express*, 2017, **25**, 25071–25078.
46 A. S. Saadeldin, M. F. O. Hameed and E. M. Elkaramany, Highly sensitive terahertz metamaterial sensor, *IEEE Sens. J.*, 2019, **19**, 7993–7999.
47 M. Janneh, A. De Marcellis and E. Palange, Design of a metasurface-based dual-band terahertz perfect absorber with very high Q-factors for sensing applications, *Opt. Commun.*, 2018, **416**, 152–159.
48 S. Banerjee, A terahertz metamaterial absorber based refractive index sensor with high quality factor, *13th International Conference on Electronics, Computers and Artificial Intelligence (ECAI)*, IEEE, 2021, pp. 1–4.